



# Archaean seafloors shallowed with age due to radiogenic heating in the mantle

Juan Carlos Rosas<sup>1,2</sup> and Jun Korenaga<sup>1</sup>

**Given the scarcity of geological data, knowledge of Earth's landscape during the Archaean eon is limited. Although the continental crust may have been as massive as present by 4 Gyr ago, the extent to which it was submerged or exposed is unclear. One key component in understanding the amount of exposed landmasses in the early Earth is the evolution of the oceanic lithosphere. Whereas the present-day oceanic lithosphere subsides as it ages, based on numerical models of mantle convection we find that higher internal heating due to a larger concentration of radioactive isotopes in the Archaean mantle halted subsidence, possibly inducing seafloor shallowing before 2.5 Gyr ago. In such a scenario, exposed landmasses in the form of volcanic islands and resurfaced seamounts or oceanic plateaus can remain subaerial for extended periods of time, and may have provided the only stable patches of dryland in the Archaean. Our results therefore permit a re-evaluation of possible locations for the origin of life, as they provide support to an existing hypothesis that suggests that life had its origins on land rather than in an oceanic environment.**

Nucleobases were either formed under early Earth conditions<sup>1–3</sup> or had an extraterrestrial origin<sup>4</sup>. The synthesis of complex biomolecules capable of self-replication, however, involves polymerization of nucleobases into nucleotides and nucleic acids. Because polymerization requires precise thermodynamic conditions<sup>5–7</sup> that were unlikely to be prevalent in the early Earth, an understanding of the Archaean surface environment is essential when discussing possible locations for abiogenesis. At present, candidate locations include deep-sea hydrothermal vents<sup>8</sup> or warm little ponds near volcanic flanks<sup>9</sup>. Phylogenetic studies have suggested that hyperthermophilic archaea of the type found near the vents may be akin to the last universal common ancestor, suggesting that life might have arisen in these vents<sup>10</sup>. However, hyperthermophiles may just be survivors of bolide impacts in the early Earth<sup>11</sup>, and the capacity of the vents and surroundings to sustain polymerization is still debated<sup>5–7</sup>. Warm little ponds, in turn, allow for long-term polymerization through seasonal wet–dry and/or freeze–thaw cycles<sup>12–14</sup> but require the existence of exposed landmasses<sup>15,16</sup>.

Given a limited number of geological constraints, estimating the extent of exposed landmass during the Archaean eon is difficult. A recent theoretical study that considers the co-evolution of prebiotic chemistry and surface environment suggests polymerization in warm little ponds following the delivery of nucleotides by meteorites<sup>17</sup>. Their parameterization of exposed landmass in the Archaean is, however, questionable because it assumes that the mass of exposed continents is equal to the mass of continental crust. Although it is possible that continents were as massive as present by 4 Gyr ago (Ga)<sup>18,19</sup>, the amount of exposed landmass is a function of several time-dependent parameters, such as ocean–mantle water exchange and seafloor topography<sup>20</sup>. In particular, seafloor topography in deep time is poorly understood. As newly formed seafloor moves away from a mid-ocean ridge, isostatic adjustment due to cooling from the surface results in changes in seafloor depth<sup>21</sup>, thus affecting the water capacity of ocean basins and the flooding of continents. At present, volcanic islands become seamounts owing to continuous seafloor subsidence (Fig. 1a). Subsidence then seems to

slow down when the lithosphere is 70–80 Myr old, probably owing to the onset of small-scale convection<sup>22</sup> as well as the impingement of mantle plumes<sup>23</sup>. In the Archaean, however, radiogenic heat production in the mantle was approximately four times larger than at present<sup>24</sup>. If radiogenic heating is high enough, subsidence may cease altogether and seafloor shallowing might occur, allowing seamounts and oceanic plateaus to resurface (Fig. 1b).

To assess the likelihood of exposed landmasses in the Archaean, therefore, we systematically explore the effect of radiogenic heating on bathymetry through numerical modelling. Our results suggest that seafloor shallowing is indeed possible for the bulk of the Archaean. Additionally, we also explore the effect of our new model of bathymetric evolution on the sea level, mid-ocean ridge depth and the exposed fraction of continental crust, thus providing a more comprehensive assessment of the Archaean landscape and its possible implications for the origin of life.

## Modelling seafloor bathymetry

To model the evolution of seafloor topography, we integrate the two-dimensional (2D) thermal convection equations with temperature-dependent viscosity and radiogenic heating using a finite-element approach<sup>25</sup>. The running time is 500 Myr. Our strategy consists of calculating 2D ridge-parallel thermal evolution and then horizontally averaging such evolution to construct a 2D, ridge-perpendicular, mantle thermal structure with a prescribed plate velocity<sup>26</sup> (Methods and Extended Data Fig. 1). Instantaneous Stoke flow is then computed for this mantle structure. Seafloor depth is calculated as:

$$w = \alpha \Delta T d \frac{\rho_m}{\rho_m - \rho_w} \frac{\sigma_{zz}|_{z'=0}}{Ra}, \quad (1)$$

where  $w$  is subsidence with respect to zero-age seafloor,  $\alpha$  is thermal expansivity (set as  $3 \times 10^{-5} \text{ K}^{-1}$ ),  $\Delta T$  is mantle potential temperature (1,350 K at present),  $d$  is mantle thickness (2,900 km),  $\rho_m$  is surface mantle density ( $3,300 \text{ kg m}^{-3}$ ),  $\rho_w$  is density of water ( $1,000 \text{ kg m}^{-3}$ ),

<sup>1</sup>Department of Earth and Planetary Sciences, Yale University, New Haven, CT, USA. <sup>2</sup>Departamento de Geofísica Aplicada, Centro de Investigación Científica y de Educación Superior de Ensenada, Ensenada, Mexico. ✉e-mail: [juanrb@cicese.mx](mailto:juanrb@cicese.mx); [jun.korenaga@yale.edu](mailto:jun.korenaga@yale.edu)

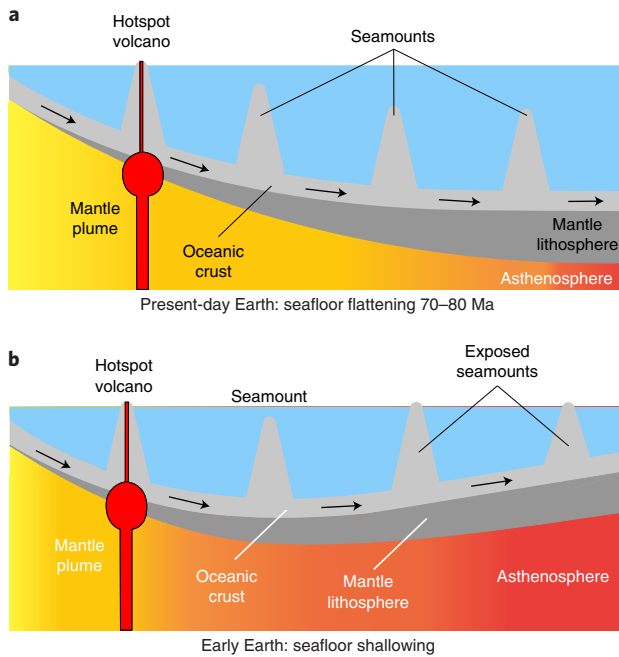


**Fig. 1 | Bathymetric evolution of oceanic lithosphere at present and in the early Earth. a**, At present, seafloor subsides as the plate moves away from mid-ocean ridge. Hotspot volcanism forms oceanic islands that eventually become seamounts as the plate subsides. Low concentration of heat-producing elements in the mantle lead to a moderate increase in temperature (yellow–red shading). **b**, In the early Earth, the concentration of heat-producing elements in the mantle was considerably higher than present, leading to a greater temperature increase. As at present, oceanic islands may become seamounts, but additional heating can lead to seafloor shallowing and allow seamounts to resurface.

$\sigma_{zz}^*|_{z^*=0}$  is the non-dimensional normal stress at the surface, and  $Ra = \alpha \rho_0 g \Delta T d^3 / \eta_0 \kappa$  is the Rayleigh number, for which  $\rho_0$  is reference density ( $4,000 \text{ kg m}^{-3}$ ),  $\kappa$  is thermal diffusivity ( $10^{-6} \text{ m}^2 \text{ s}^{-1}$ ),  $g$  is gravitational acceleration ( $9.8 \text{ m s}^{-2}$ ) and  $\eta_0$  is the reference asthenospheric viscosity. We vary  $\eta_0$  within the range  $10^{19}$ – $10^{20} \text{ Pa s}$ , consistent with geophysical observations<sup>27</sup>; we assume that the present-day asthenospheric viscosity is also valid for the Archaean, based on the likely effect of global water cycle on mantle viscosity<sup>28</sup>. The viscosity structure of the mantle is computed using realistic temperature dependence with an activation energy of  $300 \text{ kJ mol}^{-1}$  (Methods).

We measure the effect of radiogenic heating by varying the heating rate per unit mass,  $H$ , and comparing the subsidence with that predicted by the case with  $H = 0$ . Before the onset of sublithospheric convection, the latter case is equivalent to seafloor subsidence as predicted by the half space cooling (HSC) model with no radiogenic heating ( $w_{\text{hs}}$ ), given by:

$$w_{\text{hs}} = 2\alpha\Delta Td \frac{\rho_m}{\rho_m - \rho_w} \left( \frac{\kappa\tau}{\pi} \right)^{1/2}, \quad (2)$$

where  $\tau$  is the age of the lithosphere<sup>21</sup>. The range of  $H$  is from  $2.1 \times 10^{-12} \text{ W kg}^{-1}$  at present to  $8.5 \times 10^{-12} \text{ W kg}^{-1}$  at the Hadean–Archaean boundary (4 Ga), as calculated from the present concentrations of K (102 ppm), U (9.7 ppb) and Th (30 ppb) in the depleted mantle<sup>24</sup>.

### Effect of radiogenic heating and mantle viscosity on seafloor bathymetry

Seafloor bathymetry is most sensitive to radiogenic heating, with  $H > 0$  leading to slower seafloor subsidence than that predicted by

the HSC model (Fig. 2a–c). Seafloor shallowing is inferred from our model throughout the Archaean when the oceanic lithosphere is  $\sim 50$ – $100 \text{ Myr}$  old. As  $H$  decreases, shallowing also decreases, and by 1.7 Ga the seafloor is continuously subsiding. On the contrary, whereas variations in asthenospheric viscosity have a noticeable effect on the onset of sublithospheric convection (with decreasing viscosity leading to an earlier onset time), the overall evolution of a subsidence curve for a given  $H$  does not change noticeably when the viscosity is in the range of  $10^{19}$ – $10^{20} \text{ Pa s}$ , suggesting seafloor shallowing probably occurred in the early Earth regardless of the value of  $\eta_0$ .

More realistic models may be explored by employing depth-dependent profiles for heat generation and viscosity. Depth-dependent heat generation results from the melting of the mantle, which partitions heat-producing elements into the oceanic crust. We employ depleted mantle concentrations of K, U and Th, as before, from which we calculate three profiles for three ages: present, 2.5 Ga and 4 Ga (Fig. 2d). For each case, we assume that all heat-producing elements partition into the crust, leaving behind an entirely depleted ( $H = 0$ ) mantle lithosphere. The concentration of heat-producing elements in the crust is calculated from the expected thicknesses for the crust and the mantle lithosphere at each age (7 and 70 km, respectively, at present; 29 and 137 km at 2.5 Ga; and 19 and 106 km at 4 Ga, as calculated from the thermal history of the upper mantle<sup>29</sup> and a mantle melting model<sup>30</sup>). For the viscosity profile, several geophysical observations suggest that the lower mantle may be  $\sim 10$ – $30$  times more viscous, on average, than the upper mantle<sup>27</sup>. We constructed two viscosity profiles with a 10-fold and 30-fold increase in lower mantle viscosity, in addition to the purely temperature-dependent case (Fig. 2e). For the asthenospheric viscosity, we employ  $\eta_0 \approx 3 \times 10^{19} \text{ Pa s}$ .

For a given age, bathymetry for models with depth-dependent  $H$  is roughly comparable to that predicted by models with uniform  $H$  (Fig. 2f). This suggests that dynamic topography reflects the aggregated heat content in the subsurface, thereby being insensitive to the details of vertical distribution; this is consistent with the topography kernel (the sensitivity of topography to the internal density structure) expected for the suboceanic mantle<sup>31</sup>. The lower-mantle viscosity partially modulates the effect of radiogenic heating on bathymetry. At low  $H$ , the model is mostly cooling from above and density changes are located within the lithosphere only. Dynamic topography thus remains insensitive to the viscosity structure of the convective interior. As  $H$  increases, however, the effect of the viscosity of the lower mantle becomes noticeable. A general trend is that a higher value of lower-mantle viscosity consistently gives deeper seafloor, although the difference introduced by the 30-fold increase in the lower mantle is  $< 1 \text{ km}$  at most in the Hadean–Archaean boundary. This trend is also consistent with how the topography kernel is influenced by depth-dependent viscosity<sup>31</sup>. Overall, using depth-dependent profiles of heat generation and viscosity does not noticeably affect the bathymetry with respect to models with uniform profiles.

### Archaean surface environment and the origin of life

The models above highlight the effect of radiogenic heating on seafloor depth. Moreover, the high concentration of heat-producing elements in the early mantle suggest that seafloor shallowing was possible before 2.5 Ga. We now model the Archaean surface environment by tracking the evolution of sea level, ridge depth and the exposed fraction of continents. For this, we use a recent freeboard model developed to investigate the global water cycle<sup>20</sup>.

Our freeboard model assumes isostatic balance across ocean basins and continents. Secular changes in continental lithospheric buoyancy are allowed<sup>32</sup>, as well as changes in seafloor bathymetry through either HSC bathymetry or the bathymetry with radiogenic heating (RH bathymetry). To facilitate modelling, we

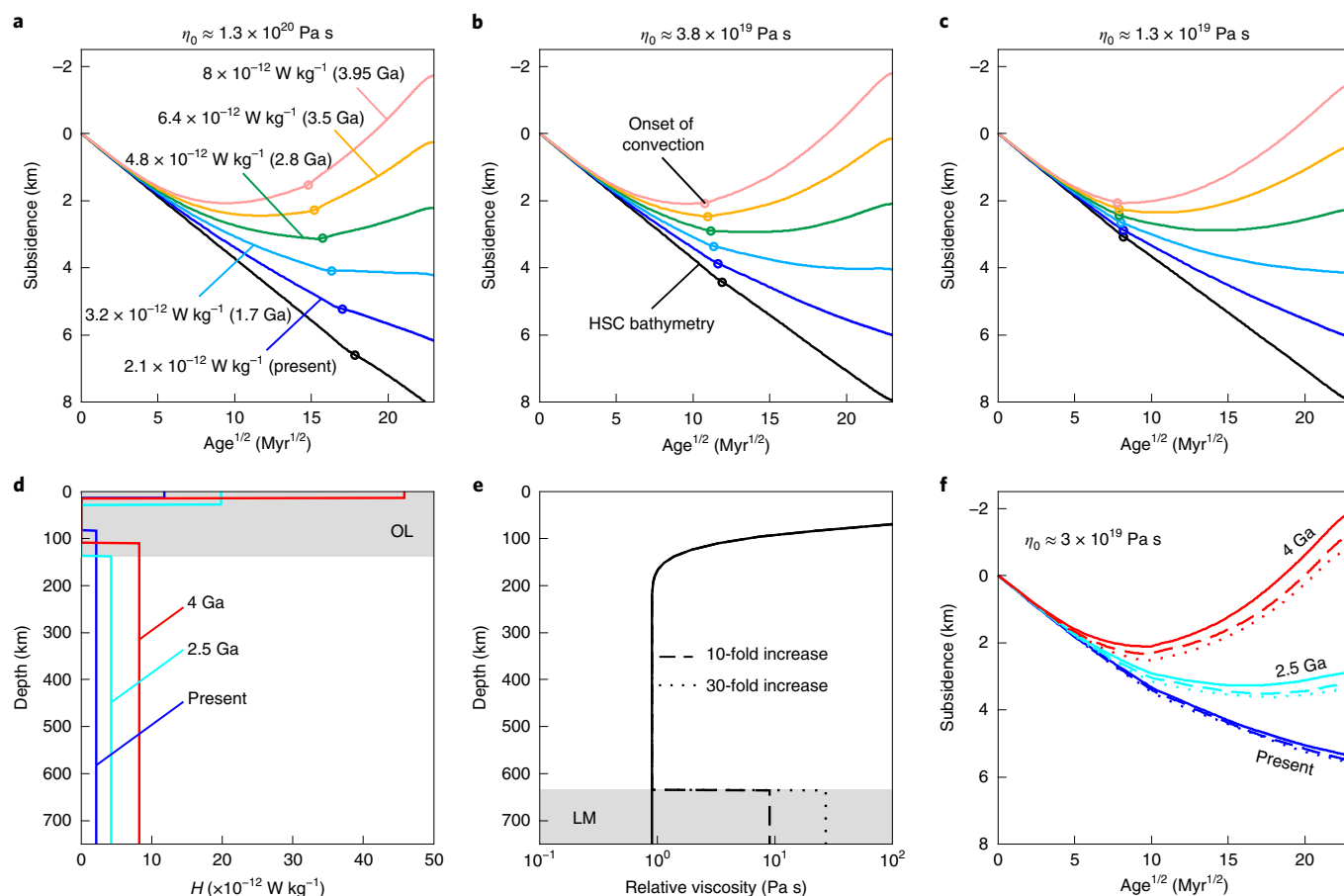


**Fig. 2 | Effect of radiogenic heating and mantle viscosity on seafloor bathymetry. a–c,** Seafloor subsidence as a function of time<sup>1/2</sup> for different values of asthenospheric viscosity ( $\eta_0$ ) and heat production ( $H$ ) at different ages, based on the geochemical model of the depleted mantle<sup>24</sup>. HSC bathymetry and onset time of sublithospheric convection (circles) are shown. **d,** Depth-dependent radiogenic heating due to mantle melting at present, 2.5 Ga and 4 Ga. The oceanic lithosphere (OL; 2.5 Ga model only) is divided into the depleted lithospheric mantle (with no heat production) and oceanic crust. **e,** Viscosity profiles with a linearly exponential form of temperature-dependent viscosity in the upper mantle (Methods). For the lower mantle (LM), we explore 10-fold (dashed line) and 30-fold (dotted line) increases in viscosity with respect to the upper mantle. **f,** Seafloor subsidence with depth-dependent radiogenic heating and viscosity. Colour coding and line type are as in **d** and **e**.

parameterize the RH bathymetry through an empirical scaling law for  $w$ , expressed as a function of  $H$  (Methods, equation (16) and Extended Data Figs. 2 and 3). Our modelling strategy closely follows that of ref. <sup>20</sup>, but the following two input parameters are worth some detailed account: the continental growth function and the ocean–mantle water flux due to subduction.

The growth of continents is parameterized through:

$$M_c(t) = \frac{M_c(t_p)}{1 - e^{-\kappa_g(t_p - t_s)}} [1 - e^{-\kappa_g(t - t_s)}], \quad (3)$$

where  $M_c$  is the continental mass,  $t_s$  is the time when crustal growth started (4.51 Ga),  $t_p$  is the present time measured from the beginning of the solar system (4.567 Ga),  $M_c(t_p)$  is the present continental mass ( $2.09 \times 10^{22}$  kg) and  $\kappa_g$  is a growth constant<sup>18</sup>. By adjusting  $\kappa_g$ , we can explore a wide range of crustal growth scenarios. We test two models:  $\kappa_g = 17$ , representing a rapid continental growth in the Hadean; and  $\kappa_g = 0.5$ , representing a gradual growth of the continents (Fig. 3a). The rapid growth model is consistent with the evolution of the samarium–neodymium isotope systems<sup>18</sup> as well as the degassing history of argon<sup>19</sup>. The gradual growth model is tested here to assess the effects of growth rate on landscape evolution. As for the ocean–mantle water flux, we constrain it by selecting a constant value that keeps the sea level approximately stable up to 2.5 Ga, consistent

with the geological record<sup>20,33</sup>. Net water flux in the ocean–mantle system has various sources and sinks, including water loss by subducting slabs (in sediments, the crust and lithospheric mantle), magmatic output from mid-ocean ridges, hotspots and arcs, and non-magmatic up-dip transport from slab to oceans. Considerable uncertainties exist even when estimating the present-day water flux<sup>34,35</sup>. Yet, using a constant value of net water influx is justified a posteriori, as a long-term average that can reproduce a steady sea level, at least back to 2.5 Ga. It should be stressed that, even with non-zero water flux, sea level can remain constant owing to changes in the relative buoyancy of continental lithosphere with respect to that of oceanic lithosphere<sup>20,32</sup>. Positive net water flux indicates more voluminous oceans in the past. Other model parameters are the same as in the reference case of the original freeboard study<sup>20</sup>. For the models presented here, we assume the continuous operation of plate tectonics<sup>28</sup> with a decrease in plate velocity in the past. With the effect of mantle melting on viscosity (that is, dehydration stiffening), a hotter mantle in the past is expected to convect more slowly, thus leading to slower plate tectonics<sup>30</sup>. Such a dynamic has been shown to be consistent with a range of geological records including the life spans of passive margins<sup>36</sup>, the cooling history of the upper mantle<sup>29</sup> and the evolution of continental plate velocities<sup>37,38</sup>.

Most studies place the present net ocean–mantle water flux at  $<10 \times 10^{14}$  g yr<sup>-1</sup> (refs. <sup>20,34,35,39,40</sup>), although it could be as large as

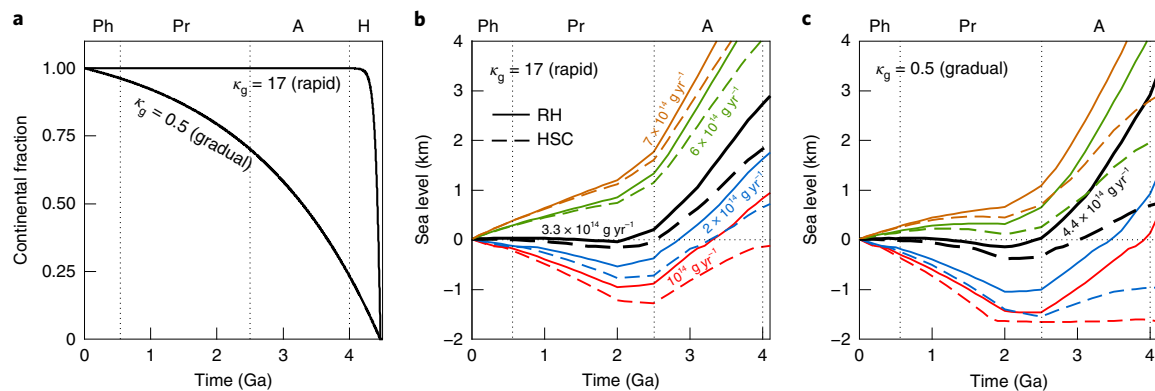


**Fig. 3 | Sea level as a function of continental growth and ocean-mantle water flux.** **a**, Rapid and gradual continental growth models (equation (3)). Vertical dotted lines divide the history of Earth into Hadean (H), Archaean (A), Proterozoic (Pr) and Phanerozoic (Ph). **b,c**, Evolution of sea level with respect to present for the rapid (**b**) and gradual (**c**) growth models, using RH (equation (1)) and HSC (equation (2)) bathymetries, for different ocean-mantle water fluxes. The selected water fluxes (black) are  $3.3 \times 10^{14} \text{ g yr}^{-1}$  and  $4.4 \times 10^{14} \text{ g yr}^{-1}$ , respectively. These water fluxes give an ocean mass of  $-2.2 \times 10^{24} \text{ g}$  (rapid growth) and  $-2.5 \times 10^{24} \text{ g}$  (gradual growth) 2.5 Ga, assuming a present-day ocean mass of  $-1.4 \times 10^{24} \text{ g}$ .

$18 \times 10^{14} \text{ g yr}^{-1}$  (ref. <sup>35</sup>). In this study,  $3.3 \times 10^{14} \text{ g yr}^{-1}$  and  $4.4 \times 10^{14} \text{ g yr}^{-1}$  are required to satisfy the constancy of sea level from 2.5 Ga to present for the rapid and gradual growth models, respectively (Fig. 3b,c), in relative agreement with the most recent estimates<sup>20,39</sup>. With these fluxes, ridge depth was deeper in the past (Fig. 4a,e). Continents become more flooded with RH bathymetry than with HSC bathymetry because the former leads to shallower seafloor, and thus a higher sea level (Fig. 4b,f). Additionally, a more gradual growth of continents means that the ocean basins would have been wider in the past, being able to hold more water and resulting in less continental flooding.

Hypsometry snapshots through the Archaean and at present are shown in Fig. 4c,d for RH bathymetry. During the early Archaean, as the tempo of plate tectonics was slower<sup>20,28</sup>, the maximum age of oceanic lithosphere is extended and seafloor shallowing is more likely to occur. By 2.5 Ga, flattening is still appreciable. For the present-day case, because the bathymetry is better approximated by the plate cooling model<sup>41</sup>, we also consider this case. For both growth models, the RH and plate model hypsometries are approximately equal, indicating the accuracy of our approach. In comparison, using HSC bathymetry results in continuous seafloor subsidence throughout the Archaean (Fig. 4g,h).

Although the chosen model for continental growth does have an impact on the size of ocean basins and thus on sea level, seafloor shallowing occurs for both rapid and gradual growth. This result is particularly important; because the rapid and gradual growth models could be considered end-member scenarios for other intermediate growth models that have been proposed<sup>42</sup>, seafloor shallowing in the Archaean is expected to persist regardless of the details of continental formation. The results presented here, therefore, are robust enough to provide a picture of an Archaean landscape in which the seafloor shallows up and submerged seamounts and oceanic plateaus may resurface (Fig. 1).

The existence of dryland in the Archaean is compatible with a number of origin-of-life models<sup>14,15</sup>, and the results presented here provide geological support to such theories. Unequivocal evidence of life has been dated at 3.5 Ga<sup>43</sup>, although the record may be pushed back to the late Hadean or early Archaean ( $\sim 4 \text{ Ga}$ )<sup>44</sup>. During this period, our results indicate that continents were fully submerged (Fig. 4b,f). As we assume a time-independent water influx, this part of our modelling results is subject to greater uncertainties compared with the Proterozoic part. The mantle at  $>2.5 \text{ Ga}$  is likely to have been hotter than that at  $<2.5 \text{ Ga}$ <sup>29</sup>, and net water influx can

be more reduced in the Archaean<sup>39</sup>. Even if the net water influx is reduced by half during the Archaean, however, continents are still expected to have been fully submerged (Fig. 3b,c). Also, temporal topographic elevation by continent–continent collision is expected to be limited because of hot crustal geotherm in the Archaean<sup>45</sup>, and this effect is already included in our freeboard modelling<sup>20</sup>. This may be used to argue that the synthesis of the first prebiotic compounds probably occurred in an aquatic environment, such as near hydrothermal vents. The formation of primitive RNA-like molecules, however, requires polymerization of nucleotides<sup>46</sup>, and the vent's surroundings are probably not well suited for this. High water temperature near the vents<sup>5</sup> and low concentration of phosphorous compounds and nitrogen oxides in the primitive ocean<sup>6,7</sup> are considered to be limiting factors. The very presence of water may also be problematic, because water tends to degrade polymerization and inhibit the formation of nucleotides through hydrolysis. Although it is possible for polymers to form with the aid of mineral surfaces<sup>47</sup> or within pore space near the vents<sup>48</sup>, the results we present here permit us to consider warm little ponds as an alternative location. The synthesis of organic compounds is achievable in these ponds through wet–dry and freeze–thaw cycles<sup>13,14</sup>, or through geochemical reactions such as serpentinization of ultramafic igneous rocks<sup>15</sup>. Even with continents submerged, seafloor shallowing due to radiogenic heating would ensure that any volcanic islands formed on sufficiently old seafloor or resurfaced seamounts and oceanic plateaus would be long-lived (Fig. 1b), providing the exposed landmass that is required for warm little ponds to exist. What is promising about this new possibility is that, whereas the spatial extent of such oceanic islands and plateaus may be limited, the tendency of these landmasses to remain subaerial is robust, as it is supported by the long-term mantle-scale heating. Considering the thermodynamic limitations of deep-water hydrothermal vents as a possible site for abiogenesis, therefore, the results presented here suggest that warm little ponds are a viable location for the origin of life.

### Online content

Any methods, additional references, Nature Research reporting summaries, source data, extended data, supplementary information, acknowledgements, peer review information; details of author contributions and competing interests; and statements of data and code availability are available at <https://doi.org/10.1038/s41561-020-00673-1>.

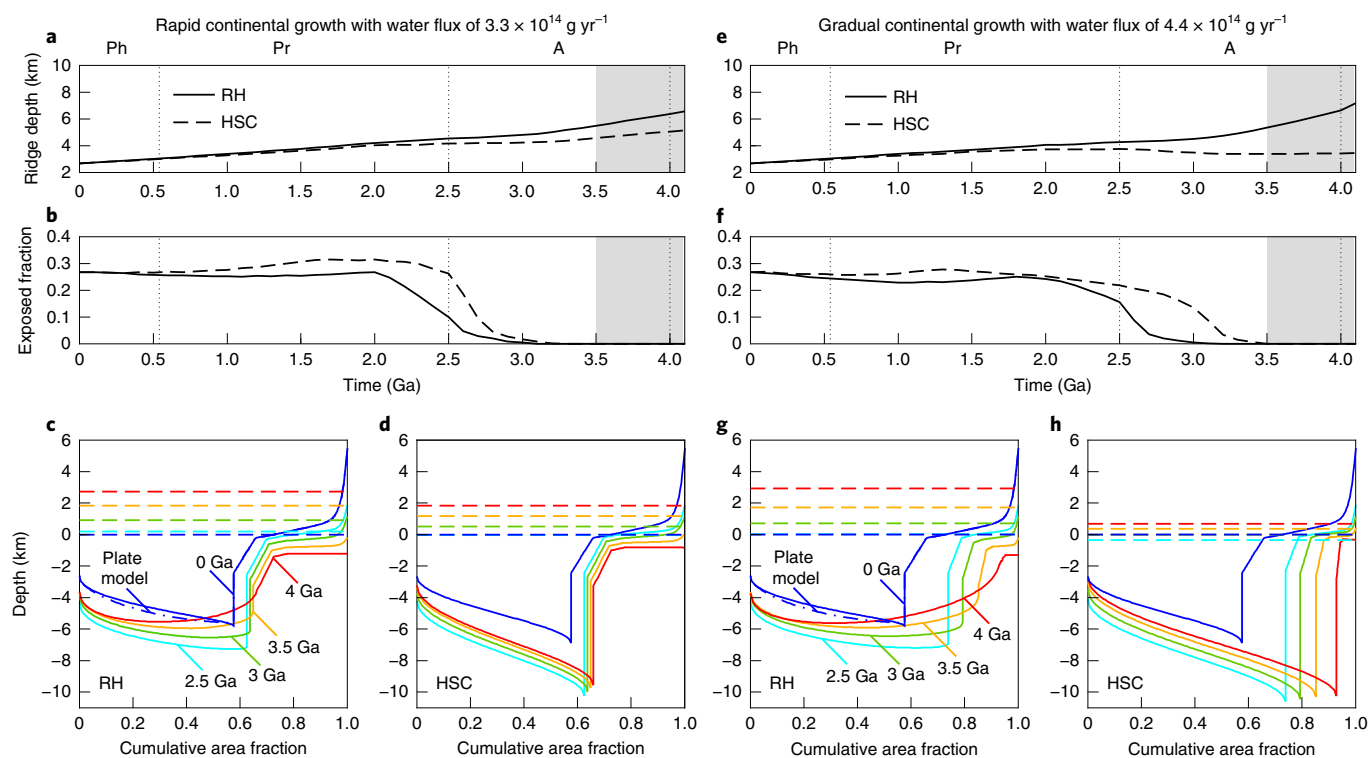


**Fig. 4 | Surface environment for rapid and gradual continental growth, with corresponding water fluxes. a, b**, Evolution of mid-ocean ridge depth (**a**) and exposed fraction of continents with respect to surface area of Earth (**b**) using RH and HSC bathymetries for rapid continental growth. Shaded region corresponds to the probable time window for the origin of life. Vertical dotted lines are as in Fig. 3. **c, d**, Hypsometry snapshots (solid lines) using RH (**c**) and HSC (**d**) at different ages for rapid continental growth. Sea levels are shown (dashed lines). Plate cooling model bathymetry is shown for present-day case (dotted-dashed line). **e-h**, As in **a-d**, but using gradual continental growth.

Received: 13 November 2019; Accepted: 24 November 2020;  
Published online: 4 January 2021

## References

- Miller, S. L. A production of amino acids under possible primitive Earth conditions. *Science* **117**, 528–529 (1953).
- Lazcano, A. & Bada, J. L. The 1953 Stanley L. Miller experiment: fifty years of prebiotic organic chemistry. *Orig. Life Evol. Biosph.* **33**, 235–242 (2003).
- Bada, J. L. New insights into prebiotic chemistry from Stanley Miller's spark discharge experiments. *Chem. Soc. Rev.* **42**, 2186–2196 (2013).
- Chyba, C. & Sagan, C. Endogenous production, exogenous delivery and impact-shock synthesis of organic molecules: an inventory for the origins of life. *Nature* **355**, 125–132 (1992).
- Miller, S. L. & Bada, J. L. Submarine hot springs and the origin of life. *Nature* **334**, 609–611 (1988).
- Mulkidjanian, A. Y., Bychkov, A. Y., Dibrova, D. V., Galperin, M. Y. & Koonin, E. V. Origin of first cells at terrestrial, anoxic geothermal fields. *Proc. Natl Acad. Sci. USA* **109**, E821–E830 (2012).
- Ranjan, S., Todd, Z. R., Rimmer, P. B., Sasselov, D. D. & Babbitt, A. R. Nitrogen oxide concentrations in natural waters on early Earth. *Geochem. Geophys. Geosyst.* **20**, 2021–2039 (2019).
- Martin, W., Baross, J., Kelley, D. & Russell, M. J. Hydrothermal vents and the origin of life. *Nat. Rev. Microbiol.* **6**, 805–814 (2008).
- Peretó, J., Bada, J. L. & Lazcano, A. Charles Darwin and the origin of life. *Orig. Life Evol. Biosph.* **39**, 395–406 (2009).
- Weiss, M. et al. The physiology and habitat of the last universal common ancestor. *Nat. Microbiol.* **1**, 16116 (2016).
- Sleep, N. H. Geological and geochemical constraints on the origin and evolution of life. *Astrobiology* **18**, 1199–1219 (2018).
- Benner, S. A., Kim, H. J. & Carrigan, M. A. Asphalt, water, and the prebiotic synthesis of ribose, ribonucleosides, and RNA. *Acc. Chem. Res.* **45**, 2025–2034 (2012).
- Mutschler, H., Wochner, A. & Holliger, P. Freeze–thaw cycles as drivers of complex ribozyme assembly. *Nat. Chem.* **7**, 502–508 (2015).
- Damer, B. A field trip to the Archaeon in search of Darwin's warm little pond. *Life* **6**, 21 (2016).
- Benner, S. A., Kim, H. J., Kim, M. J. & Ricardo, A. Planetary organic chemistry and the origins of biomolecules. *Cold Spring Harb. Perspect. Biol.* **2**, a003467 (2010).
- Bada, J. L. & Korenaga, J. Exposed areas above sea level on Earth >3.5Gyr ago: implications for prebiotic and primitive biotic chemistry. *Life* **8**, 55 (2018).
- Pearce, B. K. D., Pudritz, R. E., Semenov, D. A. & Henning, T. K. Origin of the RNA world: the fate of nucleobases in warm little ponds. *Proc. Natl Acad. Sci. USA* **114**, 11327–11332 (2017).
- Rosas, J. C. & Korenaga, J. Rapid crustal growth and efficient crustal recycling in the early Earth: implications for Hadean and Archean geodynamics. *Earth Planet. Sci. Lett.* **494**, 42–49 (2018).
- Guo, M. & Korenaga, J. Argon constraints on the early growth of felsic continental crust. *Sci. Adv.* **6**, 21 (2020).
- Korenaga, J., Planavsky, N. J. & Evans, D. A. D. Global water cycle and the coevolution of the Earth's interior and surface environment. *Philos. Trans. R. Soc. A* **375**, 20150393 (2017).
- Turcotte, D. L. & Schubert, G. *Geodynamics* (Cambridge Univ. Press, 2002).
- Parsons, B. & McKenzie, D. Mantle convection and the thermal structure of the plates. *J. Geophys. Res.* **83**, 4485–4496 (1978).
- Sleep, N. H. Small-scale convection beneath oceans and continents. *Chi. Sci. Bull.* **56**, 1292–1317 (2011).
- Korenaga, J. Pitfalls in modeling mantle convection with internal heat production. *J. Geophys. Res.* **122**, 4064–4085 (2017).
- Korenaga, J. & Jordan, T. H. Physics of multiscale convection in Earth's mantle: onset of sublithospheric convection. *J. Geophys. Res.* **108**, 2333 (2003).
- Korenaga, J. in *The Interdisciplinary Earth: A Volume in Honor of Don L. Anderson* (eds Gillian, F. R. et al.) 167–185 (Geological Society of America, 2015).
- Hager, B. in *Glacial Isostasy, Sea Level and Mantle Rheology* (eds Sabadini, R. et al.) 493–513 (American Geophysical Union, 1991).
- Korenaga, J. Initiation and evolution of plate tectonics on Earth: theories and observations. *Annu. Rev. Earth Planet. Sci.* **41**, 117–151 (2013).
- Herzberg, C., Condie, K. & Korenaga, J. Thermal history of the Earth and its petrological expression. *Earth Planet. Sci. Lett.* **292**, 79–88 (2010).
- Korenaga, J. in *Archean Geodynamics and Environments* (eds Benn, K. et al.) 7–32 (American Geophysical Union, 2006).

31. Korenaga, T. & Korenaga, J. Evolution of young oceanic lithosphere and the meaning of seafloor subsidence rate. *J. Geophys. Res.* **121**, 6315–6332 (2016).
  32. Servali, A. & Korenaga, J. Oceanic origin of continental mantle lithosphere. *Geology* **46**, 1047–1050 (2018).
  33. Bindeman, I. N. et al. Rapid emergence of subaerial landmasses and onset of a modern hydrologic cycle 2.5 billion years ago. *Nature* **557**, 545–548 (2018).
  34. Ito, E., Harris, D. M. & Anderson, A. T. Alteration of oceanic crust and geologic cycling of chlorine and water. *Geochim. Cosmochim. Acta* **47**, 1613–1624 (1983).
  35. Jarrard, R. D. Subduction fluxes of water, carbon dioxide, chlorine, and potassium. *Geochem. Geophys. Geosyst.* **4**, 8905 (2003).
  36. Bradley, D. C. Passive margins through Earth history. *Earth Sci. Rev.* **91**, 1–26 (2008).
  37. Condie, K., Pisarevsky, S. A., Korenaga, J. & Gardoll, S. Is the rate of supercontinent assembly changing with time? *Precambrian Res.* **259**, 278–289 (2015).
  38. Pehrsson, S. J., Eglinton, B. M., Evans, D. A. D., Huston, D. & Reddy, S. M. in *Supercontinent Cycles Through Earth History* (eds Li, Z. X. et al.) 83–94 (Geological Society of London, 2016).
  39. Magni, V., Bouilhol, P. & van Hunen, J. Deep water recycling through time. *Geochem. Geophys. Geosyst.* **15**, 4203–4216 (2014).
  40. van Keken, P. E., Hacker, B. R., Syracuse, E. M. & Abers, G. A. Subduction factory: 4. Depth-dependent flux of H<sub>2</sub>O from subducting slabs worldwide. *J. Geophys. Res.* **116**, B1 (2011).
  41. Stein, C. A. & Stein, S. A model for the global variation in oceanic depth and heat flow with lithospheric age. *Nature* **359**, 123–129 (1992).
  42. Korenaga, J. Crustal evolution and mantle dynamics through Earth history. *Philos. Trans. R Soc. A* **376**, 20170408 (2018).
  43. Walter, M. R., Buick, R. & Dunlop, J. S. R. Stromatolites 3,400–3,500 Myr old from the North Pole area, Western Australia. *Nature* **284**, 443–445 (1980).
  44. Bell, E. A., Boehnke, P., Harrison, T. M. & Mao, W. L. Potentially biogenic carbon preserved in a 4.1 billion-year-old zircon. *Proc. Natl Acad. Sci. USA* **112**, 14518–14521 (2015).
  45. Rey, P. F. & Houseman, G. Lithospheric scale gravitational flow: the impact of body forces on orogenic processes from Archaean to Phanerozoic. *Geol. Soc. Lond. Spec. Publ.* **253**, 153–167 (2006).
  46. Deamer, D. W. & Georgiou, C. D. Hydrothermal conditions and the origin of cellular life. *Astrobiology* **15**, 1091–1095 (2015).
  47. Burcar, B. T. et al. RNA oligomerization in laboratory analogues of alkaline hydrothermal vent systems. *Astrobiology* **15**, 509–522 (2015).
  48. Baaske, P. et al. Extreme accumulation of nucleotides in simulated hydrothermal pore systems. *Proc. Natl Acad. Sci. USA* **104**, 9346–9351 (2007).
- Publisher's note** Springer Nature remains neutral with regard to jurisdictional claims in published maps and institutional affiliations.
- © The Author(s), under exclusive licence to Springer Nature Limited 2021

## Methods

**Model description.** All models share the following boundary conditions and properties. Surface temperature is set to zero and the bottom boundary is insulated. The top and bottom boundaries are free slip, and a reflecting boundary condition is applied to the sides. Time and temperature are non-dimensionalized by  $d^2/\kappa$  and  $\Delta T$ , respectively, where  $d$  is model depth,  $\kappa$  is thermal diffusivity and  $\Delta T$  is the difference between initial and surface temperature. Non-dimensional variables are denoted with an asterisk. The aspect ratio is set to 4, and the model is discretized into 257 horizontal and 93 vertical nodes. Whereas the horizontal nodes are distributed uniformly, we concentrate 40 of the 93 vertical nodes in the shallowest part of the model ( $z^* \geq 0.8$ , where  $z^*$  is height and  $z^* = 1$  is the top surface) to better capture the dynamics of sublithospheric convection (that is, growth and instability of the upper thermal boundary layer).

We employ a linearized version of the Arrhenius-type of temperature-dependent viscosity, given by:

$$\eta^*(T^*) = \exp[\theta(1 - T^*)], \quad (4)$$

where  $\eta^*$  is normalized by reference (that is, asthenospheric) viscosity,  $\eta_0$ , defined at  $T^* = 1$  and  $\theta$  is the Frank-Kamenetskii parameter<sup>49</sup>, which is related to the activation energy,  $E$ , as:

$$\theta = \frac{E\Delta T}{R(T_s + \Delta T)^2}, \quad (5)$$

where  $R$  is the universal gas constant and  $T_s = 273$  K is the surface temperature. The Rayleigh number is defined as:

$$Ra = \frac{\alpha\rho_0 g \Delta T d^3}{\eta_0 \kappa}, \quad (6)$$

where  $\alpha$  is thermal expansivity ( $3 \times 10^{-5} \text{ K}^{-1}$ ),  $\rho_0$  is reference density ( $4,000 \text{ kg m}^{-3}$ ) and  $g$  is gravitational acceleration ( $9.8 \text{ m s}^{-2}$ ). Finally, heat generation rate per unit mass ( $H$ ) is non-dimensionalized by:

$$H^* = \left( \frac{\rho_0 d^2}{k\Delta T} \right) H, \quad (7)$$

where  $k = 4 \text{ W m}^{-1} \text{ K}^{-1}$  is thermal conductivity.

Our models are fully described by the three non-dimensional parameters  $\theta$ ,  $Ra$  and  $H^*$ . We employ  $\theta = 18.5$  for all our models, consistent with  $E = 300 \text{ kJ mol}^{-1}$  for the upper mantle<sup>50</sup>. Such a value for  $\theta$  remains approximately constant in the deep time because of the limited variation of  $\Delta T$  (1,350 K at present). The asthenospheric viscosity is set between  $10^{19}$  Pa s and  $10^{20}$  Pa s, corresponding to  $Ra \approx 3 \times 10^8 - 3 \times 10^9$ . The range of  $H^*$  is between 0 and 50, corresponding to  $H = 0 - 8.5 \times 10^{-12} \text{ W kg}^{-1}$  (see 'Modelling seafloor bathymetry'). Because the bottom boundary is insulated, our models are purely internally heated and do not incorporate the effect of upwelling mantle plumes, thus allowing us to focus on the dynamics of the ocean lithosphere exclusively.

Our modelling strategy is as follows<sup>26</sup>. We run a convection model for a given set of  $Ra$  and  $H^*$  for a duration of 500 Myr. Depth-dependent profiles for  $H^*$  and viscosity (Fig. 2d,e) may also be employed. At each time step, we calculate a horizontally averaged temperature profile from 2D ridge-parallel simulation (Extended Data Fig. 1a-c) and assemble them to create a ridge-perpendicular thermal structure profile with a prescribed plate velocity (Extended Data Fig. 1d). Instantaneous Stokes flow is then computed. Dynamic seafloor topography (that is, topography due to mantle motions) along our trench-perpendicular thermal structure is proportional to the normal stress acting on the surface,  $\sigma_{zz}|_{z=0}$ :

$$\sigma_{zz}|_{z=0} = \alpha\rho_0 g w. \quad (8)$$

Equation (1) may then be obtained by non-dimensionalizing the normal stress by  $\eta_0 \kappa / d^2$  in equation (8) and multiplying by the topographic scale  $\alpha \Delta T d \rho_m / (\rho_m - \rho_w)$ . Seafloor subsidence is then converted to a function of seafloor age using the prescribed plate velocity. It should be noted that equation (1), when applied to a model with  $H = 0$ , recovers the bathymetry predicted by the half space cooling model (equation (2)).

**Empirical scaling law for seafloor subsidence.** To apply our model of bathymetric evolution to our freeboard model, however, we develop an empirical scaling law for seafloor subsidence by using the results from our generic models (Extended Data Fig. 2) and analysing the deviation of modelled seafloor depth ( $w$ ; equation (1)) with respect to the seafloor depth as calculated from the HSC model ( $w_{\text{hs}}$ ; equation (2)). We define this deviation as:

$$\delta w = \frac{w_{\text{hs}} - w}{w_{\text{hs}}}. \quad (9)$$

Seafloor depth deviates from that predicted by the HSC model as internal heating increases (Extended Data Fig. 2a). Because sublithospheric convection affects subsidence after the onset time ( $t_c$ ), we construct our empirical scaling law

by approximating the evolution of  $\delta w$  during the conductive (that is, before onset time) and convective phases through linear trends. For the conductive phase, the linear trend is given by:

$$\delta w_1 = m_1(t^{1/2} - t_i^{1/2}), \quad (10)$$

where  $m_1$  is the slope and  $t_i^{1/2} \approx 2.5 \text{ Myr}^{1/2}$  is the intersection with the horizontal axis (Extended Data Fig. 2a). The subscript 1 refers to the conductive phase. The slope is a function of  $H^*$  (Extended Data Fig. 2b) and it may be found from the following linear fit:

$$m_1 = a_1 H^*, \quad (11)$$

where  $a_1 = 0.001$ . Substituting equations (9) and (11) into equation (10), the empirical scaling law for the seafloor subsidence during the conductive phase is given by:

$$w_1 = w_{\text{hs}}[1 - a_1 H^*(t^{1/2} - t_i^{1/2})]. \quad (12)$$

Similarly, the linear trend for the evolution of  $\delta w$  after the onset of convection is given by:

$$\delta w_2 = \delta w_1(t_c) + m_2(t^{1/2} - t_c^{1/2}), \quad (13)$$

where the subscript 2 refers to the convective phase and the slope  $m_2$  is given by:

$$m_2 = \frac{\delta w_2(t_{\text{max}}) - \delta w_1(t_c)}{t_{\text{max}}^{1/2} - t_c^{1/2}}. \quad (14)$$

In equation (14), the maximum running time is set at  $t_{\text{max}} = 500$  Myr. For  $\delta w_2(t_{\text{max}})$ , we notice that the final seafloor depth for a given amount of radiogenic heating is approximately the same for all reference viscosity (that is, Rayleigh number) values (Fig. 2a-c). We can thus express  $\delta w_2(t_{\text{max}})$  as a function of  $H^*$  only (Extended Data Fig. 2c), and the data may be fitted by:

$$\delta w_2(t_{\text{max}}) = a_2 H^* + b_2, \quad (15)$$

where  $a_2 = 0.0228$  and  $b_2 = 0.0452$ . We may find  $\delta w_2$  from equations (12)–(15). Our empirical scaling law for seafloor subsidence throughout 500 Myr ( $w_s$ ) is thus a piecewise function of the form:

$$w_s = w_{\text{hs}} \times \begin{cases} 1 - a_1 H^*(t^{1/2} - t_i^{1/2}), & t < t_c \\ 1 - a_1 H^*(t_c^{1/2} - t_i^{1/2}) + \frac{H^*[a_1(t_c^{1/2} - t_i^{1/2}) - a_2] - b_2}{t_{\text{max}}^{1/2} - t_c^{1/2}}(t^{1/2} - t_c^{1/2}), & t_c \leq t \leq t_{\text{ma}} \end{cases} \quad (16)$$

where  $t_c$  may be calculated from previously derived scaling laws<sup>25</sup>.

The difference between the subsidence as calculated from equation (1) and through our empirical scaling remains relatively low (below 250 m) for all values of  $Ra$  and  $H^*$  (Extended Data Fig. 3). Because our empirical scaling is based on the analytical HSC bathymetry model, seafloor subsidence may be readily calculated for any given value of radiogenic heating through equation (16), allowing us to bypass the instantaneous Stokes flow calculation on which our modelling results are constructed.

## Data availability

Data used for figures in the main text and Methods are generated by our convection and freeboard computer codes. We have been unable to share these data due to the substantial size of the data files. Computer code to generate data files, however, is available upon request to the corresponding authors.

## Code availability

Computer code is available upon request to the corresponding authors.

## References

- Solomatov, V. S. & Moresi, L. N. Scaling of time-dependent stagnant lid convection: application to small-scale convection on Earth and other terrestrial planets. *J. Geophys. Res.* **105**, 21795–21817 (2000).
- Karato, S. & Wu, P. Rheology of the upper mantle: a synthesis. *Science* **260**, 771–778 (1993).

## Acknowledgements

We are grateful to K. Rogers, L. Williams and R. Hernandez for their help and assistance while preparing this manuscript. This material is based upon work supported in part by two grants from the US National Aeronautics and Space Administration: (1) through the NASA Astrobiology Institute under Cooperative Agreement No. NNA15BB03A, and (2) under Cooperative Agreement No. 80NSSC19M0069, both issued through the Science Mission Directorate. This material is also supported by the US National Science Foundation under grant EAR-1753916.

**Author contributions**

J.C.R. performed the calculations and wrote the manuscript. J.K. designed the project, discussed the results and commented on the manuscript.

**Competing interests**

The authors declare no competing interests.

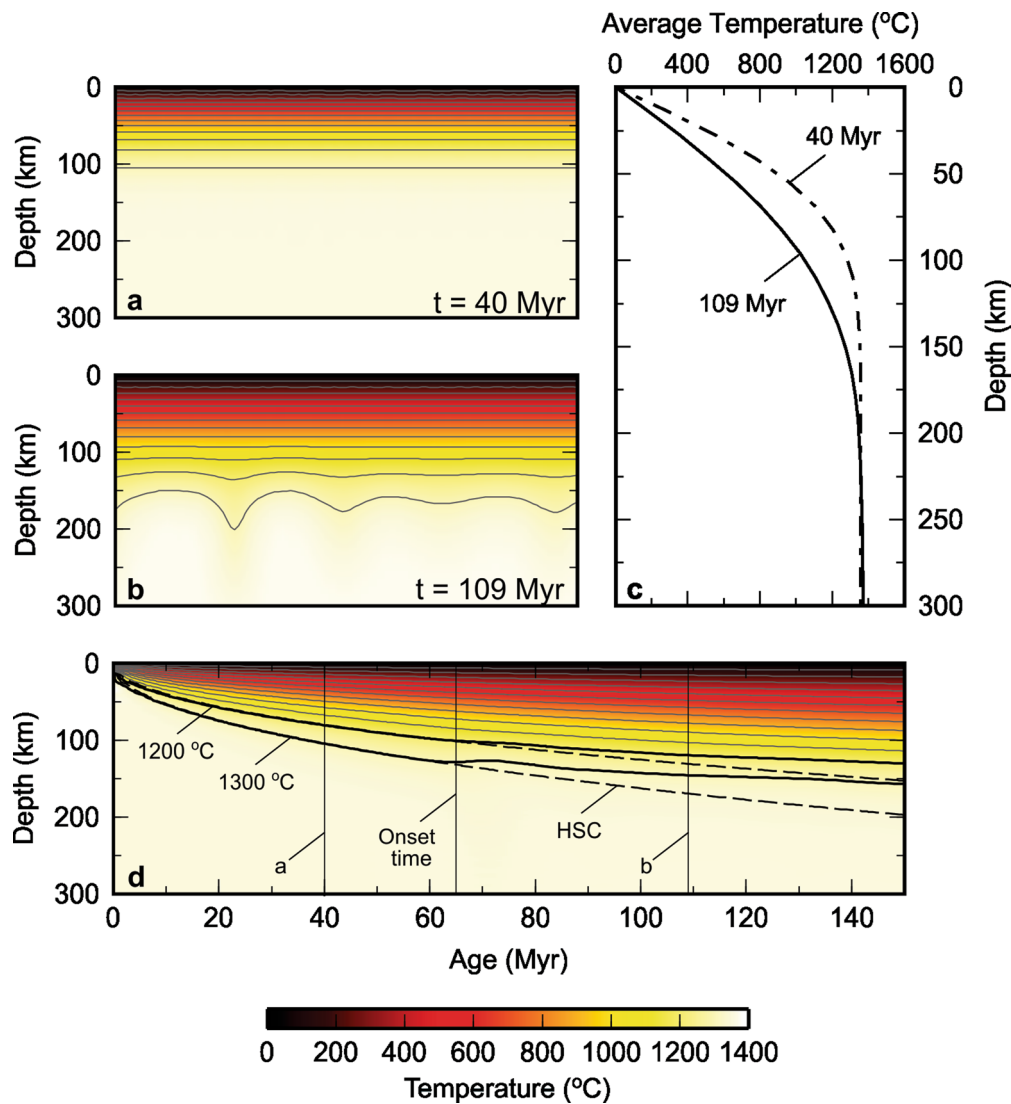
**Additional information**

**Extended data** is available for this paper at <https://doi.org/10.1038/s41561-020-00673-1>.

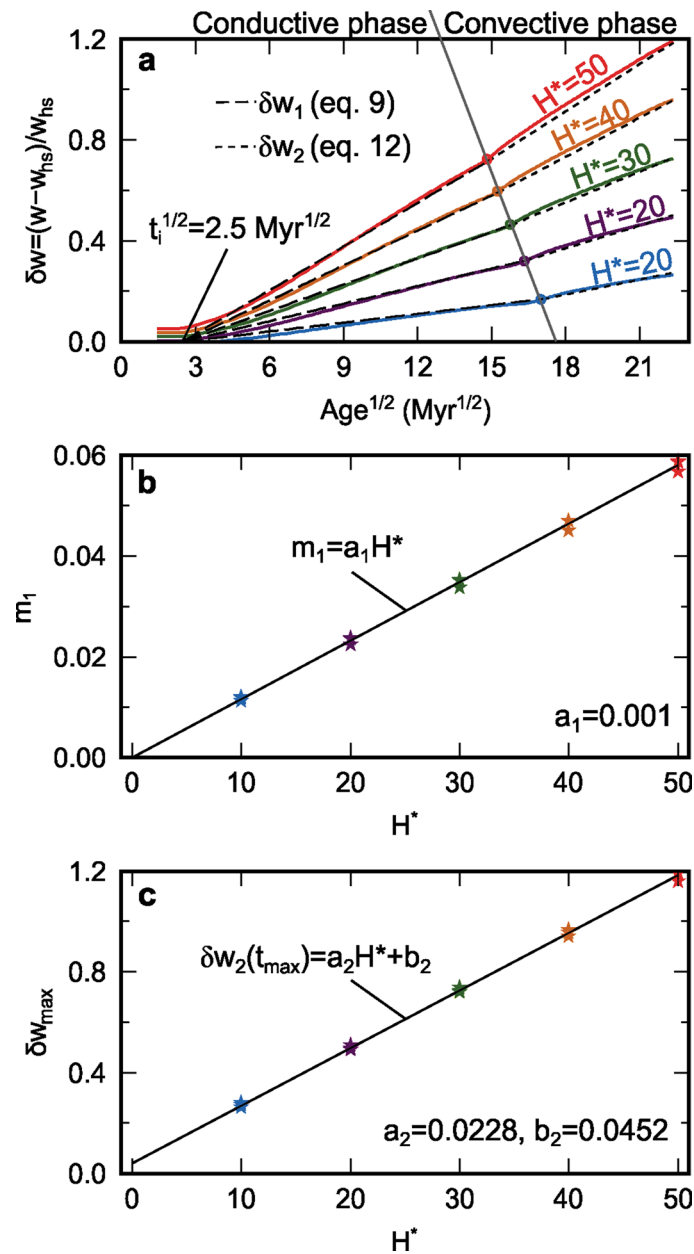
**Correspondence and requests for materials** should be addressed to J.C.R. or J.K.

**Peer review information** *Nature Geoscience* thanks Norman Sleep and the other, anonymous, reviewer(s) for their contribution to the peer review of this work. Primary Handling Editor: Rebecca Neely.

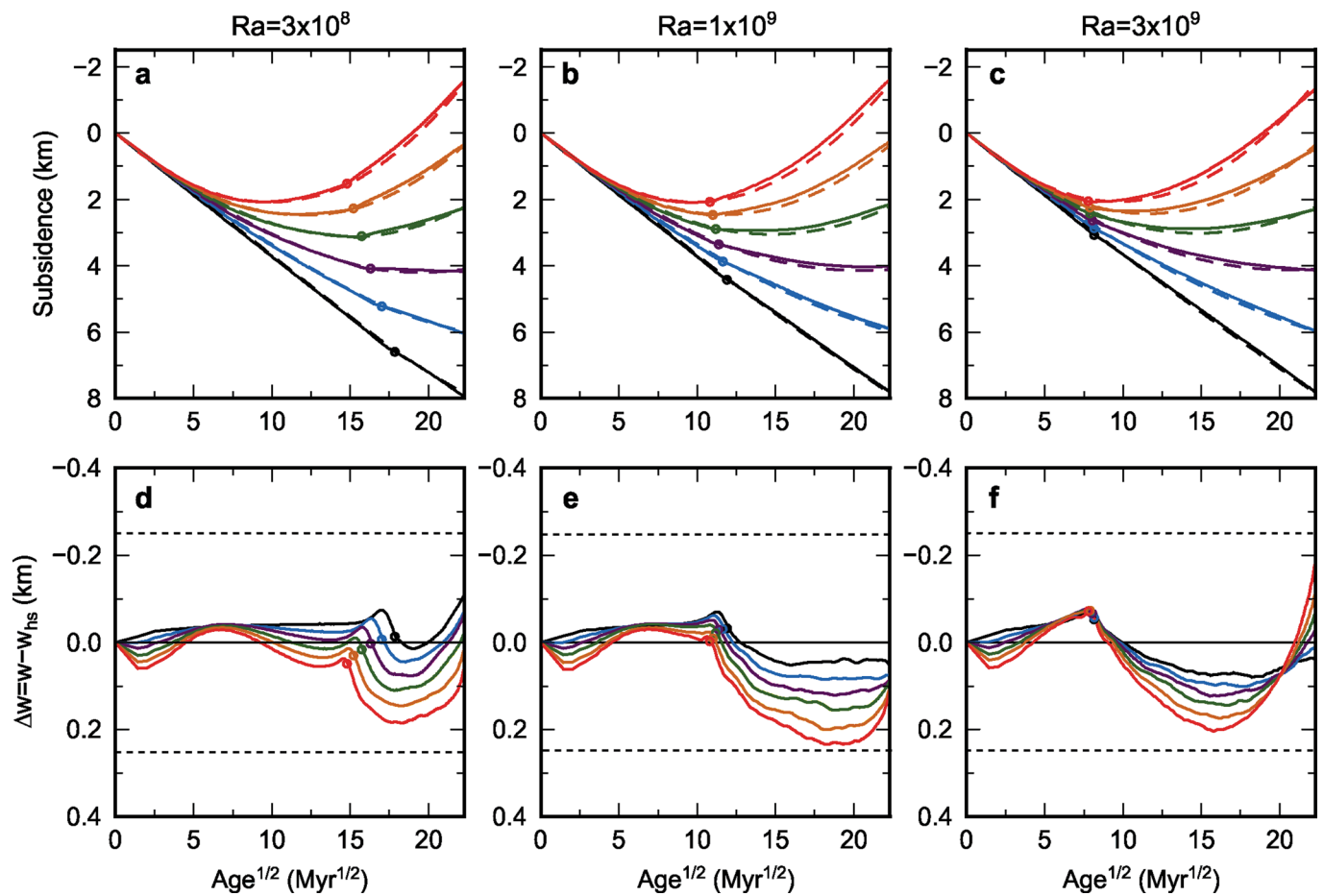
**Reprints and permissions information** is available at [www.nature.com/reprints](http://www.nature.com/reprints).



**Extended Data Fig. 1 | Modelling strategy.** Numerical results of a model with  $Ra = 3 \times 10^9$  ( $\eta_0 \approx 1.3 \times 10^{19}$  Pa s) and  $H' = 13.2$  ( $H = 2.12 \times 10^{-12}$  W kg $^{-1}$ ), appropriate for present-day Earth. **a-b:** Snapshots of uppermost section of temperature field 40 Ma and 109 Ma, before and after onset of convection, respectively, with temperature contours at an interval of 100° C. **c:** Horizontally averaged temperature profiles for snapshots **a** and **b**. **d:** Ridge-perpendicular thermal structure constructed by assembling horizontally averaged temperature profiles for every time step. Subsidence may then be calculated by computing instantaneous Stokes flow and applying Equation (1). Location of temperature profiles **a** and **b**, as well as the onset time, are shown. Isotherms of 1200° C and 1300° C as calculated using radiogenic heating (RH; solid) and half space cooling (HSC; dashed) bathymetries are highlighted. before onset time, thermal structure of radiogenic heating model resembles that predicted by HSC model.



**Extended Data Fig. 2 | Subsidence deviation.** **a:** Evolution of  $\delta w$  for models with different values of  $H^*$  and  $Ra = 3 \times 10^8$ . Models are divided into conductive and convective phases at onset time, with each phase being fitted by a linear trend ( $\delta w_1$  and  $\delta w_2$ , respectively). For any  $H^*$ ,  $\delta w_1$  intersects the horizontal axis at  $t_i^{1/2} = 2.5 \text{ Myr}^{1/2}$ . **b-c:** Slope of  $\delta w_1$  (**b**) and  $\delta w_2$  at  $t_{\max} = 500 \text{ Myr}$  (**c**) as a function of  $H^*$ . Linear trends are given by  $m_1 = a_1 H^*$  in **b**, where  $a_1 = 0.001$ , and by  $\delta w_2(t_{\max}) = a_2 H^* + b_2$  in **c**, where  $a_2 = 0.0228$  and  $b_2 = 0.0452$ . Colour coding as in **a**.



**Extended Data Fig. 3 | Comparison between modelled bathymetry and empirical scaling law.** **a-c:** Modelled seafloor subsidence for models with  $Ra = 3 \times 10^8$  (**a**),  $Ra = 1 \times 10^9$  (**b**) and  $Ra = 3 \times 10^9$  (**c**), respectively (solid). Colour coding as in Extended Data Figure 2. Seafloor subsidence as predicted from empirical scaling law is also shown (equation 16; dashed). **d-f:** Difference between modelled seafloor subsidence and empirical scaling for  $Ra = 3 \times 10^8$  (**d**),  $Ra = 1 \times 10^9$  (**e**) and  $Ra = 3 \times 10^9$  (**f**), respectively. Colour coding as in **a**. Zero-difference level is shown (thin horizontal line). Difference never exceeds 250 m (dashed horizontal lines).